Selection of inertial modes in spherical Couette flow

Douglas H. Kelley,[*] Santiago Andrés Triana, and Daniel S. Zimmerman

*Department of Physics and Institute for Research in Electronics and Applied Physics, University of Maryland, College Park,
Maryland 20742, USA*

Daniel P. Lathrop

*Departments of Physics and Geology, Institute for Research in Electronics and Applied Physics, and Institute for Physical Science
and Technology, University of Maryland, College Park, Maryland 20742, USA*

Spherical Couette flow involves fluid sheared between concentric coaxially rotating spheres. Its scientific relevance lies not only in the simplicity of the system but also in its applicability to astrophysical objects such as atmospheres, oceans, and planetary cores. One common behavior in all rotating flows, including spherical Couette flow, is the presence of inertial modes, which are linear wave modes restored by the Coriolis force. Building on a previous identification of inertial modes in a laboratory spherical Couette cell, here we propose selection mechanisms to explain the presence of the particular modes we have observed. Mode selection depends on both amplification and damping. Our experimental observations are consistent with amplification and selection by over-reflection at a shear layer, and we would expect other spherical Couette devices to behave similarly. Damping effects, due in part to the presence of an inner sphere, add further constraints which are likely to play a role in mode selection in planetary atmospheres and cores, including the core of earth.

I. INTRODUCTION

Comprised of fluid contained between an inner sphere and a concentric outer spherical shell, spherical Couette flow has a simple geometry in which inertia, viscosity, rotation, and shear interact to yield an intricate set of linear and nonlinear instabilities. Spherical Couette flow bears further relevance because of its broad geophysical applications—planetary cores and atmospheres are well modeled as spherical shells. Its behaviors, however, are not as well understood as those of its cousin, Taylor-Couette flow, and theoretical predictions are more difficult to make since a spherical shell of appreciable thickness cannot be approximated as two dimensional.

One behavior nearly universal in fluids with global rotation is inertial waves. Their occurrence can be explained by writing the Navier-Stokes equation, which governs fluid momentum, in a frame rotating with the fluid,

$$\frac{\partial \boldsymbol{u}}{\partial t} + (\boldsymbol{u} \cdot \boldsymbol{\nabla})\boldsymbol{u} = -\frac{1}{\rho} \boldsymbol{\nabla} P + \nu \nabla^2 \boldsymbol{u} - 2\boldsymbol{\Omega} \times \boldsymbol{u}, \quad (1)$$

where $\boldsymbol{u}$ is the fluid velocity, t is time, ρ is the fluid density, P is the reduced pressure (which includes both the usual pressure forces and the centrifugal forces), ν is the kinematic viscosity of the fluid, and $\boldsymbol{\Omega}$ is the bulk rotation rate vector. The last term accounts for the Coriolis force that arises because of rotation and has primary importance when rotation is rapid. Considering a fluid that is incompressible ($\boldsymbol{\nabla} \cdot \boldsymbol{u} = 0$) and seeking small-amplitude motions for which viscosity is unimportant [30], we can reduce Eq. (1) to

$$\frac{\partial}{\partial t} \boldsymbol{\nabla} \times \boldsymbol{u} = 2(\boldsymbol{\Omega} \cdot \boldsymbol{\nabla})\boldsymbol{u}, \quad (2)$$

which admits wave solutions of the form $\boldsymbol{u} = \tilde{\boldsymbol{u}} \exp i(\boldsymbol{k} \cdot \boldsymbol{r} + \omega t)$, provided that the waves are transverse and that they obey the peculiar dispersion relation (e.g., see [1])

$$\omega = 2\hat{\boldsymbol{k}} \cdot \boldsymbol{\Omega}. \quad (3)$$

Here $\tilde{\boldsymbol{u}}$ is a vector constant, $\boldsymbol{k}$ is the wave vector, $\hat{\boldsymbol{k}} = \boldsymbol{k}/|\boldsymbol{k}|$ is the unit wave vector, $\boldsymbol{r}$ is the position vector, and ω is the wave frequency in the rotating frame. Being the solutions to Eq. (2), inertial waves are the linear eigenmodes of any rapidly rotating, inviscid ($\nu = 0$) fluid, and likely to arise in any system well approximated as such.

In an infinite body of rotating fluid, inertial waves exist at all frequencies (up to twice the bulk rotation rate) as plane waves in space, constrained only by Eq. (3). Adding boundaries imposes a further constraint and yields a set of inertial *modes*. In a full sphere of inviscid fluid [31], those modes are known analytically [2–4] and are countably infinite, with discrete frequencies and rotational symmetries. Each mode can be uniquely identified by three quantities; we shall use spatial degree, spatial order, and normalized temporal frequency $(l, m, \omega/\Omega)$, respectively. Here $\Omega = |\boldsymbol{\Omega}|$, and the degree l and order m are symmetry numbers having the same meaning as in spherical harmonic notation. Though the inertial modes in a sphere are not spherical harmonics, they have common boundary requirements (periodicity) and can thus be characterized with the same nomenclature.

Since Eq. (3) still applies, each mode has a characteristic angle that relates simply to its frequency,

---

*Present address: Department of Mechanical Engineering, Yale University; douglas.kelley@yale.edu
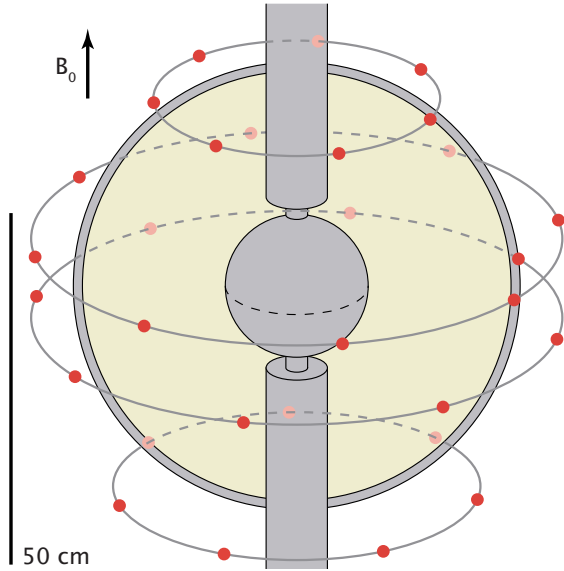
FIG. 1. (Color online) Our experimental device. Liquid sodium fills the gap between the inner solid sphere and the outer spherical shell. Driven by separate ac motors, the two boundaries rotate independently. A steady axial magnetic field B_0 is imposed externally. Each dot marks the location of a Hall probe, 30 of which are mounted on four axial rings in an arrangement favorable for projection onto the vector spherical harmonics. The probes are oriented in the direction of the cylindrical radius (horizontal and toward the axis).

$$\theta_c = \arccos(\omega/2\Omega). \tag{4}$$

The characteristic angle is an important geometrical description of the mode. At latitudes equal to θ_c, the Coriolis acceleration equals the modal acceleration, and a sort of resonance occurs [5]. In the inviscid limit, the local velocity scales as $1/\sqrt{d}$, where d is the distance to the characteristic latitude [6]. With viscosity, the singularities [7] become "eruptions" in the viscous boundary layer, causing it to detach and form a conical, free shear layer at an angle θ_c with respect to the axis of rotation [6,8,9]. A pressure singularity appears at θ_c in calculations that neglect the nonlinear terms [10], which become essential at that latitude. Our discussion will return to θ_c below.

We have previously identified inertial modes in spherical Couette flow [11] using an experimental apparatus similar to the one shown in Fig. 1. In it, fluid is contained between an outer, spherical shell with diameter $b=60$ cm, rotating at the rate Ω_o; and an inner, solid sphere with diameter $a=20$ cm, rotating at the rate Ω_i. Each of these two boundaries is driven by a 7.5 kW, ac induction motor. The test fluid is liquid sodium, which we choose for its excellent electrical conductivity, advantageous for studying hydromagnetic effects. We apply an axial steady magnetic field and use Hall probes (in the laboratory frame) to observe magnetic induction that arises from interactions between the imposed field and the flowing, conductive fluid. To be precise, the induced field is governed by the induction equation

$$\frac{\partial \boldsymbol{B}}{\partial t} = \eta \nabla^2 \boldsymbol{B} + \boldsymbol{\nabla} \times (\boldsymbol{u} \times \boldsymbol{B}), \tag{5}$$

which quickly follows from Maxwell's equations and Ohm's law, $\boldsymbol{J} = \sigma(\boldsymbol{E} + \boldsymbol{u} \times \boldsymbol{B})$. Here $\boldsymbol{B}$ is the magnetic field, $\eta = (\mu\sigma)^{-1}$ is the magnetic diffusivity of the fluid, $\boldsymbol{J}$ is the current density, σ is the conductivity of the fluid, and μ is the magnetic constant. Only one approximation is necessary: we have neglected Maxwell's displacement current, which is nearly zero as long as the fluid speed is not relativistic.

In this discussion we consider the case of a steady applied field $\boldsymbol{B}_0$ and the resulting induction $\boldsymbol{B}_1$, where $|\boldsymbol{B}_1| \ll |\boldsymbol{B}_0|$ and the flow amplitude is again small. Linearizing Eq. (5) accordingly, we can write

$$\frac{\partial \boldsymbol{B}_1}{\partial t} = \eta \nabla^2 \boldsymbol{B_1} + \boldsymbol{\nabla} \times (\boldsymbol{u} \times \boldsymbol{B_0}). \tag{6}$$

Thus the measured magnetic induction $\boldsymbol{B}_1$ gives information about the flow; in particular, a known applied field $\boldsymbol{B}_0$ and a known flow $\boldsymbol{u}$ give rise to a known induction. According to the selection rules established in [12], a flow with degree l and order m, in the presence of an axial field such as ours, gives rise to an induction pattern with degree $l \pm 1$ and order m. Our 30 Hall probes are positioned to allow us to project the observed magnetic induction onto the vector spherical harmonics up to degree and order four; thus the degree l and order m of the velocity field are immediately available. Likewise ω is readily obtained via Fourier transformation, and so we are able to identify inertial modes uniquely as they arise in the flow.

One goal of the device is to model earth's core, where the swirling flow of liquid iron is thought to self-organize and give rise to earth's magnetic field in a process known as the dynamo effect (e.g., see [13]). The radius ratio $a/b=0.33$ of our apparatus approximates the ratio of the radius of earth's inner core to the radius of its mantle [14], and the small magnetic diffusivity η of sodium intensifies hydromagnetic effects. The present discussion, however, will focus on purely hydrodynamic behaviors; here we use magnetic induction only as a passive probe, as in Eq. (6).

For reference we mention in passing that in the experiments described here, the Ekman number was on the order $E \sim 10^{-7}$ and the Rossby number lay in the range $-2 \leq \mathrm{Ro} \leq 0.75$. Both are defined below.

II. OBSERVATIONS OF INERTIAL MODES

When the rotation rate of the outer boundary is large ($\Omega_o/2\pi > 10$ Hz), differential rotation produces magnetic fields that are strongly oscillatory. One example is given in Fig. 2, which shows both the spectrum of such a signal and its time series. The field is dominated by a single temporal frequency $\omega_{\mathrm{lab}}/2\pi = 23.25$ Hz, which displays roughly four orders of magnitude more spectral power than any other frequency. Knowing this frequency and knowing the degree and order of the induction from our array of Hall probes, we can show that this intense oscillatory behavior is consistent with the presence of a $(l, m, \omega/\Omega) = (3, 2, 0.667)$ inertial mode. Moreover our colleague Tilgner has numerically calculated
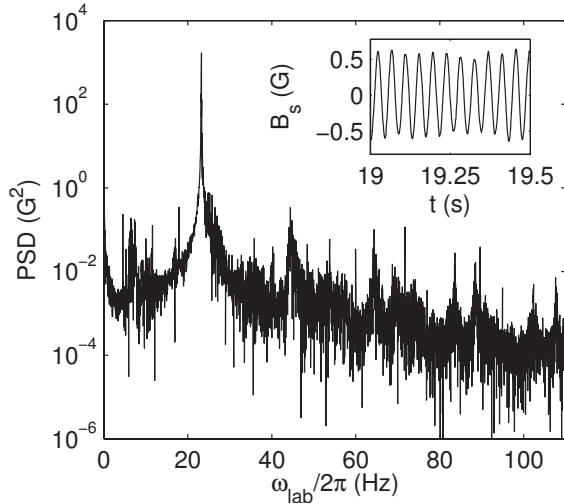
FIG. 2. Power spectral density (PSD) of the magnetic field near the equator, with $\Omega_o/2\pi = 18.0$ Hz, $\Omega_i/2\pi = 5.0$ Hz, and $B_0 = 120$ G. This spectrum is calculated from 32 s of data without averaging; a portion of the corresponding time series (with its mean removed) is shown in the inset.

the magnetic induction pattern to be expected from that analytically known mode, showing good agreement with our experimental observations. In past work we have identified seven such modes using these techniques [11]; they are listed in Table I. A question left open in the past work, which forms the core of the current discussion, is mode selection: of the infinite number of inertial modes possible in a sphere, why do these seven arise?

Each observed mode is repeatable, appearing at different outer rotation rates Ω_o as long as the Rossby number Ro $=\Omega_i/\Omega_o - 1$, a dimensionless measure of the differential rotation, remains the same; to first order, Ro controls inertial mode behavior. We can summarize that behavior with a spec-

TABLE I. Experimentally identified inertial modes. Each has a unique combination of degree l, order m, and normalized frequency ω/Ω. The characteristic angle θ_c [see Eq. (4)] and squared flux Σ [see Eq. (11)] of each is also listed. The symmetry numbers l and m describe the velocity field; modes whose velocity field has degree l produce magnetic fields with degree $l-1$, consistent with theoretical selection rules [12]. Modes whose velocity field has degree $l=6$ were detected with a probe array different from the one shown in Fig. 1, which allowed for the identification of modes of higher degree through an indirect process but was ill-suited for direct projection onto the vector spherical harmonics.

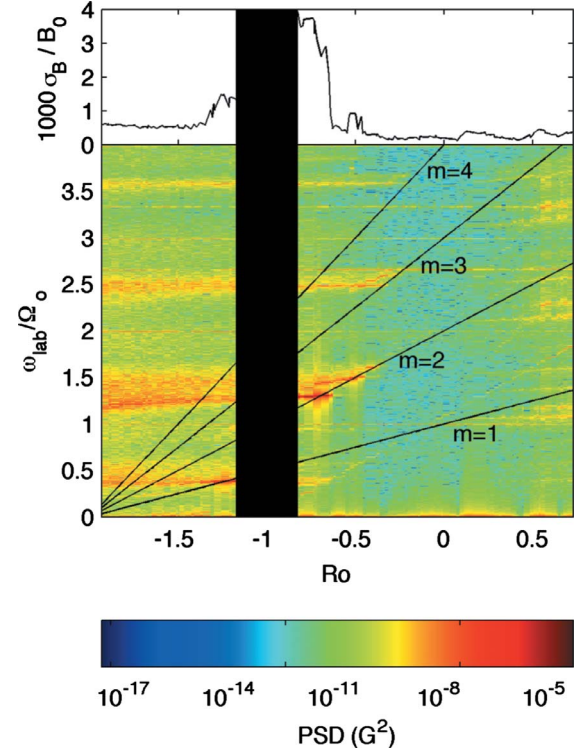| l	m	ω/Ω	θ_c	Σ
3	2	0.667	1.231	0
4	1	0.612	1.260	2.81×10^{-2}
4	3	0.500	1.318	0
5	2	0.467	1.335	2.90×10^{-3}
5	4	0.400	1.369	0
6	1	0.440	1.349	1.07×10^{-1}
6	3	0.378	1.381	3.08×10^{-4}

FIG. 3. (Color online) Magnetic field data taken from an equatorial Hall probe with $\Omega_o/2\pi = 18.0$ Hz. The lower plot is a spectrogram, with its vertical axis showing the normalized signal frequency ω_{lab}/Ω_o as measured in the laboratory frame, and its horizontal axis showing the dimensionless differential rotation Ro. Each column of pixels is a power spectrum of 32 s of data, with power indicated by the varying shades. The black central region lies at low speeds inaccessible with our ac motors. The upper plot shows the standard deviation σ_B of the same data normalized by the applied magnetic field B_0.

trogram, shown in Fig. 3, in which each column of pixels is composed of one power spectrum like the one in Fig. 2. As we vary Ro, the spectral content of the observed signal varies, often indicating inertial modes, which appear as intensely shaded regions, narrow in ω/Ω_o and persistent in Ro. Also plotted in Fig. 3 is the normalized deviation of the signal, reiterating the dominant role of inertial modes. The black lines plotted over the spectrogram will be discussed below. No inertial modes appear at Ro=0; they draw their power from shear imposed by differential rotation.

III. MODE AMPLIFICATION BY OVER-REFLECTION

In fact, our observations suggest that inertial modes draw their power from the shear via over-reflection—a claim to be explained presently. In the simplest case, when two layers of fluid flow past each other, forming a shear layer, pressure waves impinging on that shear layer can be reflected and/or transmitted, depending on the angle of wave incidence α (as measured with respect to the normal) and the normalized shear rate $M = u_{shear}/c_p$ (where u_{shear} is the velocity difference between the two layers and c_p is the wave speed). As has long been known [15], the normalized intensity of a wave reflected by a shear layer is

$$R^2 = \left(\frac{1-Z}{1+Z}\right)^2, \qquad (7)$$

where

$$Z = -\frac{\sqrt{\csc^2 \alpha + M^2 - 2M \csc \alpha - 1}}{\sin 2\alpha(\csc^2 \alpha + M^2 - 2M \csc \alpha)}. \qquad (8)$$

Though Eq. (7) was derived for acoustic waves, the necessary assumptions are few, and the results below give some support for applying it to inertial waves as well. Over-reflection is also known to exist in Rossby waves [16] (which in physical terms are essentially the same as inertial waves) and in internal gravity waves [17] [whose dispersion relation is mathematically identical to that of inertial waves, Eq. (3)].

For certain angles α, it follows from Eq. (7) that $R^2 > 1$, implying over-reflection, in which energy is transferred from the shear to the reflected wave. Perhaps more interestingly, the theory predicts the existence of angles α for which $R^2 = \infty$, as long as $M > 2$. In any physical system, additional effects not accounted for by over-reflection would cause the gain to saturate at a finite value, but we would expect large amplification nonetheless.

The physical system of our most direct interest is, of course, the one sketched in Fig. 1. We hypothesize that within it, some region of fluid rotates with the outer boundary at rate Ω_o, while some other region rotates with the inner boundary at rate Ω_i. Thus a shear layer separates the two regions. Most likely it forms on a cylinder coaxial with the rotation axis and tangent to the inner sphere at its equator, as first described by Stewartson [18] and consistent with later work in hydromagnetic flow [19]. Since we do not have direct velocity measurements, the location of the shear layer may remain a matter of speculation; even still, we can use experimental control parameters to write its normalized shear rate,

$$M = -m\frac{\Omega_o}{\omega}\text{Ro}. \qquad (9)$$

To do so we have used the azimuthal propagation speed of inertial modes, $c_p = \omega/m$. Since our Hall probes are mounted in the laboratory frame, signals with frequency ω in the rotating frame appear to the probes as signals with frequency $\omega_{\text{lab}} = m\Omega_o - \omega$. Using this mapping and rearranging Eq. (9), we can write

$$\frac{\omega_{\text{lab}}}{\Omega_o} = \frac{m}{M}\text{Ro} + m, \qquad (10)$$

which, keeping the normalized shear rate M and order m fixed, specifies that the observed frequency of a hypothetical inertial mode, excited by over-reflection, has a linear relationship to Ro. Since angles with $R^2 = \infty$ first appear at $M = 2$, we use that value as an onset condition and plot a family of lines, one for each m, on the spectrogram in Fig. 3. These boundary lines correctly predict the onset of inertial modes as observed in our experiments. Again, no induction is possible at Ro=0, where neither shear nor relative motion is imposed upon the fluid. For Ro<0, large amplification of
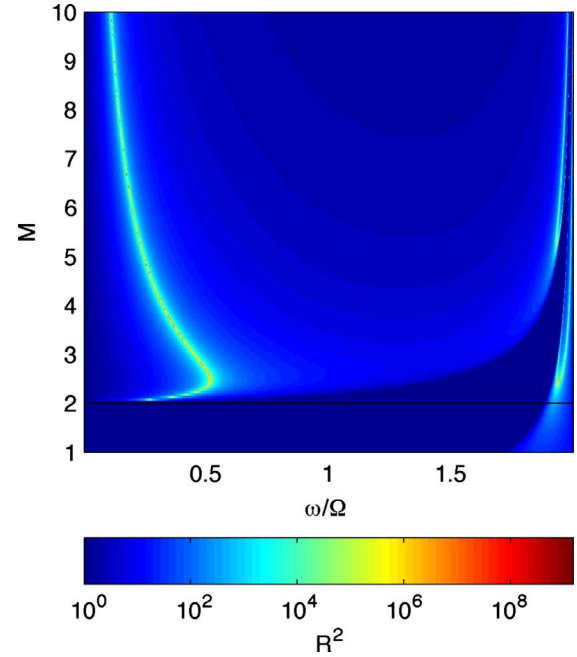

FIG. 4. (Color online) Intensity of waves reflected from a shear layer normalized by intensity of the incoming wave. Normalized intensity R^2 is plotted as a function of normalized frequency ω/Ω and normalized shear speed M. Angles at which $R^2 = \infty$ first appear at $M = 2$, marked with a solid line; see Table II.

inertial modes by over-reflection is possible only on the left side of the boundaries—that is, on the side opposite Ro=0. Consistent with this condition, we observe strong inertial modes immediately left of the boundaries and broadband induction throughout the entire region left of the boundaries. From this result we have previously asserted [11] that the inertial modes we observe draw their power from shear via over-reflection.

But Eq. (7) asserts that the normalized intensity R^2 depends not only on the normalized shear rate M but also on the angle of incidence α. Though the geometry of an inertial mode is complicated, here we shall *postulate* that the appropriate angle of incidence is the characteristic angle of the mode ($\alpha = \theta_c$) and shall show that such a hypothesis has implications for inertial mode selection which are consistent with our experimental observations.

Combining Eqs. (4) and (7), we can relate the amplification of an inertial mode by over-reflection to the normalized shear M and the frequency ω. The relationship is quantified by the plot in Fig. 4, which shows the frequencies of large (nominally infinite) gain, which we shall refer to as "critical frequencies." The original work [15] noted that infinite gain is possible but did not precisely locate it. In Table II we tabulate the normalized shear speeds where critical frequencies exist, as calculated from Eqs. (4) and (7). New critical frequencies appear in pairs reminiscent of a period doubling bifurcation. A prominent region of large gain exists at low frequencies $\omega/\Omega < 0.6$. Accordingly, the modes we have observed experimentally have frequencies in the same range (see Table I), giving preliminary support to our hypothesis $\alpha = \theta_c$.

TABLE II. Count of critical frequencies. The first critical frequency (where $R^2 = \infty$) appears at $(\omega/\Omega, M) = (0, 2)$. Others arise in pairs at (1.9359, 2.36656) and (1.9332, 5.22959). No more than five critical frequencies are present for $M \leq 100$, and it seems unlikely that more arise at any M.

Normalized shear rate	Count of critical frequencies
$0 \leq M \leq 2$	0
$2 < M \leq 2.36656$	1
$2.36656 < M \leq 5.22959$	3
$5.22959 < M$	5

Proceeding with this hypothesis, we can calculate the normalized intensity R^2 for any given inertial mode at any given normalized shear rate M. Constructing a list of all low-order ($l \leq 10$) inertial modes, we have calculated R^2 for each mode, throughout the range $1 \leq M \leq 10$. At each M, some particular mode, which we will call the "strong mode," is amplified most strongly (i.e., has the largest R^2). The frequency ω/Ω of each strong mode is plotted as a function of M in Fig. 5. We would expect the strong modes to have frequencies similar to the critical frequencies shown in Fig. 4—and they do. What we could not have predicted, however, is the dominance of the critical frequency nearest $\omega/\Omega = 0$. Though as many as five critical frequencies exist over large ranges of M, the strong modes almost always lie near the one with lowest frequency. This unexpected theoretical result is consistent with our experimental observations and gives further support to our hypothesis $\alpha = \theta_c$.

In fact, the agreement between theory and experiment goes further. Of the seven inertial modes we have identified

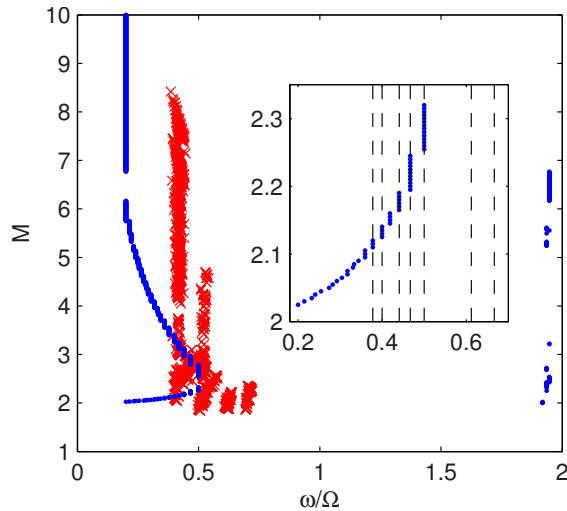FIG. 5. (Color online) Prediction from over-reflection theory of inertial mode selection. For each normalized shear speed M, the plot shows (dotted) the normalized frequency ω/Ω of the one inertial mode with $l \leq 10$ that is most strongly amplified, according to Eq. (7). The inset shows an expanded view of the region near $M = 2$, with dashed lines marking the frequencies of the seven modes we have identified experimentally. Also plotted (as Xs) are the experimental parameters where the modes listed in Table I were identified, using the same data shown in Fig. 3.

TABLE III. Strong modes over the range $2 < M \leq 2.5$, as calculated from over-reflection theory using Eq. (7). The normalized shear rate where each mode first appears, $M_{\min}$, is also listed. Experimentally identified modes, which are the lowest-order modes in the list, are marked with $\star$; compare to Table I.

l	m	ω/Ω	θ_c	$M_{\min}$
10	9	0.200	1.471	2.0228
10	7	0.214	1.463	2.0285
9	8	0.222	1.460	2.0319
10	5	0.232	1.454	2.0347
9	6	0.240	1.450	2.0378
8	7	0.250	1.446	2.0409
10	3	0.254	1.443	2.0434
9	4	0.263	1.439	2.0460
8	5	0.273	1.434	2.0499
10	1	0.282	1.429	2.0539
7	6	0.285	1.427	2.0565
9	2	0.292	1.424	2.0589
8	3	0.304	1.418	2.0632
7	4	0.317	1.411	2.0696
9	0	0.330	1.405	2.0768
6	5	0.333	1.403	2.0814
8	1	0.344	1.398	2.0854
7	2	0.359	1.390	2.0937
6	3	0.378	1.381	2.1056$\star$
5	4	0.400	1.369	2.1216$\star$
7	0	0.418	1.360	2.1402
6	1	0.440	1.349	2.1619$\star$
5	2	0.467	1.335	2.1938$\star$
9	1	1.935	0.254	2.2460
4	3	0.500	1.318	2.2547$\star$
9	1	1.935	0.254	2.3215
10	1	1.94714	0.230	2.4252

experimentally, five comprise the lowest-order strong modes near $M = 2$. All strong modes over the range $2 < M \leq 2.5$ are listed in Table III, along with the normalized shear rate $M_{\min}$ where each first appears. Since modes present in the flow with large l or m would be invisible to our Hall probe array, we have experimentally identified all the modes observable to us that over-reflection theory would predict in this range. Figure 5 also shows experimental measurements of identified modes, whose onsets are not inconsistent with $M_{\min}$ as predicted by over-reflection theory, giving further support to our hypothesis $\alpha = \theta_c$ and to the assertion that over-reflection affects mode selection. That the observed frequencies exceed the theoretical, inviscid ones by a few percent is no surprise; rather, it is predicted by viscous corrections to the theory [5,20].

Shear giving rise to wave modes via over-reflection may be related to the shear-induced oscillatory modes discussed by Chandrasekhar [21] or to the Kelvin-Helmholtz shear instability. The phenomenon also seems to bear close relationship to recent numerical studies of tidal forcing of inertial

modes in a spherical shell, in which boundary eruptions at the characteristic latitude lead to dramatic effects [22]. Using algorithms developed for that work, Rieutord was able to produce resonance curves whose highest peaks agree well with the modal frequencies we have observed experimentally. We look forward to future studies using additional predictions and/or new data that might distinguish the explanation we have made using over-reflection from other possible explanations—or might show them to be equivalent.

Meanwhile we suspect that over-reflection plays an important role in mode selection in other spherical Couette devices, as it seems to do in ours. In particular, the wave motions recently observed in the Derviche Tourneur Sodium (DTS) apparatus [23,24] may be selected by over-reflection. Mode selection by over-reflection is not likely to be the primary selection mechanism in Earth's core, however, since differential rotation of the inner core is not more than $0.5°/\text{yr}$ [25,26].

This discrepancy between nature and experiment is one way in which spherical Couette devices are imperfect models of planetary cores and deserves comment. As experimentalists we hope that many aspects of the essential physics of planetary dynamos might be elucidated despite the discrepancy but perhaps a rotating hydromagnetic spherical shell that drives motion via convection would seem more faithful. Such a device has been constructed and studied previously by Shew *et al.* [27]. However, producing flow vigorous enough to approximate the dimensionless parameters of planetary cores—especially the magnetic Reynolds number, important for magnetic behaviors such as the dynamo effect—proved to be a great challenge. In terms of that dimensionless parameter, a spherical Couette device is a more faithful model.

IV. MODE DAMPING BY BOUNDARIES

But over-reflection is not the sole selection mechanism for selection of inertial modes in spherical Couette flow, as indicated by a question we have not yet addressed: what about the other two modes? As shown in Fig. 5 and Table III, five of the seven modes we have identified experimentally are strong modes according to over-reflection theory—but the other two are not. Further detail is provided by Fig. 6, which shows the predicted gain R^2 of each identified mode as a function of M. Five of the plots show cusps where R^2 diverges, but the other two show no cusps and nearly always have lower gain. Nonetheless our observations show that these two modes are excited over wide ranges of M, as shown in Figs. 3 and 5. Thus amplification alone provides an incomplete picture of mode selection; damping must be considered as well. To say the same thing in a different way, amplification and damping are not unique mechanisms but different sides of the same coin. A similar complex interplay between forcing and damping was noted in the results of a linear stability analysis of tidal forcing [22]. Performing the same sort of calculation for spherical Couette flow might answer our questions about amplification and damping directly but that calculation is beyond the scope of the work presented here.
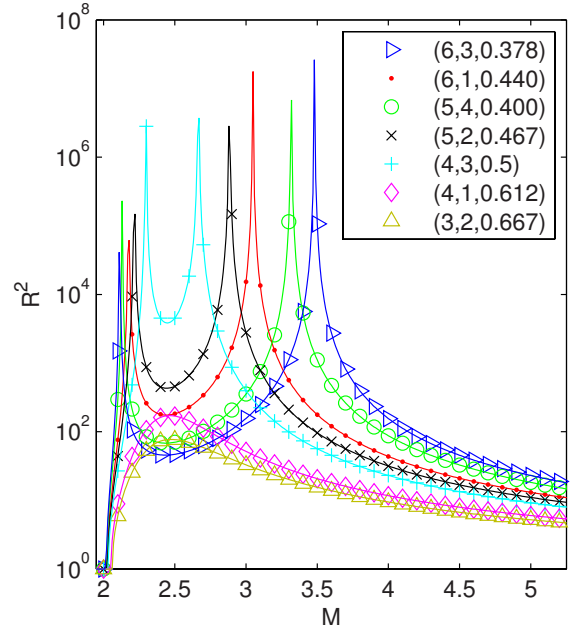

FIG. 6. (Color online) Normalized intensity R^2, calculated from Eq. (7), of the seven modes identified experimentally. Two have finite gain for all M but dominate in some parameter regimes nonetheless.

Short of that calculation, past work on damping of inertial modes may provide some insight even if it cannot answer our questions directly. For a full sphere with free-slip boundaries, inertial mode damping coefficients have been calculated both with and without a viscous correction by Greenspan [5] and by Aldridge and Toomre [20] but only for axisymmetric ($m=0$) modes without flow across the equator. By contrast, the modes we have identified are nonaxisymmetric, always have flow across the equator, and occur in a spherical shell with no-slip boundaries. Aldridge later calculated damping coefficients in a spherical shell, using a variational approach [10], but again only in the axisymmetric case. Stergiopoulos and Aldridge used experimental ringdown measurements to obtain empirical approximations of the damping coefficients of a few $m=1$ modes in a sphere with an inner boundary [28], but the inner boundary was not spherical, the modes do not match those we have identified, and the modes were chosen by tuning to their resonant frequencies—not by allowing the selected modes to dominate. Finally, Rieutord calculated the linear eigenmodes of a spherical shell with radius ratio $a/b=0.35$. Interested in earth's core, he included rotation, buoyancy, and viscosity, but the inner and outer boundaries rotate at the same rate; he did not consider spherical Couette flow.

We address damping in spherical Couette flow by beginning with a simple assertion. No analytic solution to Eq. (2) is known in a spherical shell geometry, but experiments and variational calculations [10,28] tell us that many modes which arise in a spherical shell closely resemble their counterparts in the full sphere. In fact, modes with frequency $\omega/\Omega=2/(m+1)$ exist essentially unchanged in a spherical shell [6], and three of the modes we have observed—$(l,m,\omega/\Omega)=(3,2,0.667)$, $(4,3,0.500)$, and
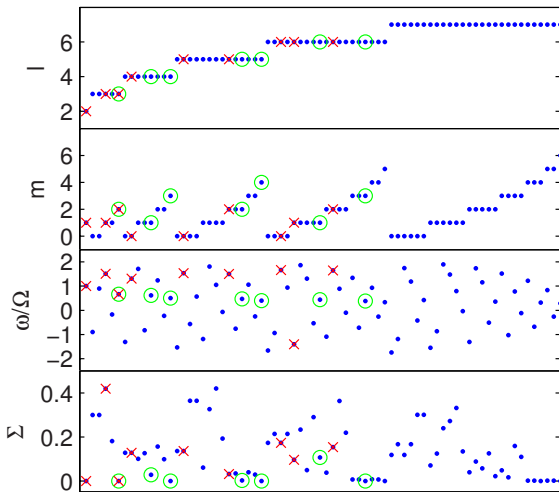
FIG. 7. (Color online) Listing of all inertial modes through $l=7$, by degree l, order m, and frequency ω/Ω, along with the normalized squared flux Σ of each. Each mode we have observed experimentally is marked with a circle, and each mode predicted in [29] (see Table IV) is marked with an X.

$(5,4,0.400)$—are members of this group. Throughout this work, the theoretical inertial modes to which we compare observations are full-sphere modes. Our simple assertion is that full-sphere modes with large flows through the region of the inner sphere are unlikely to have a close counterpart in a spherical shell. We quantify the flow through that region with the normalized mean-square flux at the inner boundary,

$$\Sigma = \frac{\int_0^\pi \int_0^{2\pi} (\boldsymbol{u} \cdot \hat{\boldsymbol{r}})^2 r^2 \sin\theta \, d\phi \, d\theta|_{r=a}}{\int_0^b \int_0^\pi \int_0^{2\pi} \boldsymbol{u}^2 r^2 \sin\theta \, d\phi \, d\theta \, dr},\tag{11}$$

where we use spherical coordinates (r,θ,ϕ) and $\hat{\boldsymbol{r}}$ is the unit vector in the radial direction. Figure 7 shows Σ for all full-sphere inertial modes with $l \le 7$, calculated using the analytical expression for each mode as given in [4]. Modes with frequency $2/(m+1)$ have $\Sigma=0$ identically. The normalized mean-square flux of the seven modes identified in experiments is listed in Table I, and those modes are also marked in Fig. 7. All have small flux ($\Sigma \le 0.11$), and six of the seven have lower flux than any other mode with the same degree l and order m; the only exception is the mode with $(l,m,\omega/\Omega)=(6,1,0.440)$, for which the flux is 0.107, while the flux is 0.050 and 0.096 for the modes $(6,1,1.306)$ and $(6,1,-1.404)$, respectively. Thus our observations are consistent with the assertion that full-sphere modes with large flows through the region of the inner sphere are unlikely to have a close counterpart in a spherical shell. This assertion also explains the fact that all the modes we observe are antisymmetric with respect to the equator. Though many of the full-sphere modes are symmetric with respect to the equator, their flux is consistently much higher than the antisymmetric modes.

The condition imposed by small flux, like the condition imposed by over-reflection, seems to be an important factor

TABLE IV. The most weakly damped inertial modes in a spherical shell as calculated in [29]. The eigenvalues λ_{rr} apply to no-slip boundaries. The mode marked with $\star$ is one of the seven we have identified experimentally; see Table I.

l	m	ω/Ω	λ_{rr}
3	1	1.5099	$-5.977 \times 10^{-3} + 0.74383i$
5	0	1.5301	$-6.095 \times 10^{-3} + 0.75200i$
2	1	1	$-6.197 \times 10^{-3} + 0.50079i$
6	1	-1.4042	$-6.744 \times 10^{-3} - 0.69936i$
4	0	1.3093	$-7.190 \times 10^{-3} + 0.66216i$
5	2	1.4964	$-7.331 \times 10^{-3} + 0.74731i$
6	0	1.6604	$-7.463 \times 10^{-3} + 0.81736i$
6	2	1.6434	$-7.593 \times 10^{-3} + 0.81308i$
3	2	0.6667	$-8.224 \times 10^{-3} + 0.33355i$ $\star$
8	0	1.3544	$-8.714 \times 10^{-3} + 0.68559i$

in mode selection. Going further to postulate that small flux is associated with small damping, we propose that the two modes $(3,2,0.667)$ and $(4,1,0.612)$ appear experimentally without ever being strong modes according to Eq. (7) because their damping is unusually low. Experimental measurements of the damping of a few inertial modes in a full sphere were obtained long ago [20] but only in the axisymmetric case, which excludes the modes we have identified. The aforementioned resonance curves, produced by Rieutord after this manuscript was first written, support our hypothesis; the highest peak for any low frequency, $m=1$ mode appears near 0.612, and the highest peak for any low frequency, $m=2$ mode appears near 0.667. Future experimental measurements of mode damping might add further support.

For comparison, we turn to the past publication that most directly addresses damping of inertial modes in spherical shells that of Rieutord [29], whose results are summarized in Table IV. It lists the ten least damped modes and their eigenvalues, calculated numerically with linear stability theory, using no-slip boundary conditions. One of the ten is the $(3,2,0.667)$ mode, which we observe experimentally, though it is not a strong mode according to over-reflection theory. Thus one past stability analysis suggests that this mode is selected by small damping, not solely by large amplification, consistent with our proposal above. Interestingly, however, there are no modes that are both strong modes according to over-reflection (Table III) and least-damped modes according to that set of calculations (Table IV).

None of the other modes predicted by [29] match the modes we have identified experimentally (compare Tables I and IV). To explain the mismatch, we begin by pointing out the different physics at work in each situation: our laboratory experiment involves large rotational forces and excitation by differential rotation, while the numerical calculations of [29] incorporate no differential rotation, use smaller rotational forces [32], and incorporate buoyancy and viscosity. However, we must revisit our assertion that full-sphere modes with large flow through the region of the inner sphere are unlikely to have close counterparts in a spherical shell. A number of the modes listed in Table IV have large flux Σ, as

plotted in Fig. 7. Though their damping rates may be low in a linear stability calculation, where by definition all perturbations have vanishing amplitude, large flow through the inner boundary cannot be sustained. We would not expect the (3,1,1.510) mode or other modes with large Σ to appear in experimental devices, in direct simulations, or in physical systems such as earth's core. The resonant curves mentioned above, calculated by Rieutord more recently than the results of [29], incorporate shear imposed by rigid boundaries and agree more closely with our experimental observations. They also show that the (4,1,0.612) mode is also damped quite weakly, as we would have expected.

V. SUMMARY

Being the linear eigenmodes of any rapidly rotating inviscid fluid inertial modes arise commonly in geophysical, astrophysical, industrial, and laboratory flows, often dominating the power spectra and flow dynamics. Theoretical methods to predict which particular modes arise could give leading-order information about those flows. We have proposed two such methods, one based on mode amplification by over-reflection and one based on damping by boundary conditions. We have compared these methods to experimental observations, showing that either method is usually consistent with our observations and that a combination of the two gives a reasonable explanation for all we have observed. Future experimental measurements of modal damping rates may shed further light on mode selection, and a recent theoretical study [22] seems to offer insights as well. Our predictions based on damping apply directly to atmospheres, planetary cores, and experiments designed to model those flows, in which rotating fluid is bounded by a spherical shell. Our predictions based on over-reflection apply to spherical Couette devices and to astrophysical objects in which differential rotation is present.

[1] L. D. Landau and E. M. Lifshitz, *Fluid Mechanics, Theoretical Physics*, 2nd ed. (Elsevier, Oxford, England, 2004).

[2] G. H. Bryan, Philos. Trans. R. Soc. London, Ser. A **180**, 187 (1889).

[3] M. D. Kudlick, Ph.D. thesis, Massachusetts Institute of Technology, 1966.

[4] K. Zhang, P. Earnshaw, X. Liao, and F. H. Busse, J. Fluid Mech. **437**, 103 (2001).

[5] H. P. Greenspan, J. Fluid Mech. **20**, 673 (1964).

[6] M. Rieutord, B. Georgeot, and L. Valdettaro, J. Fluid Mech. **435**, 103 (2001).

[7] P. H. Roberts and K. Stewartson, Astrophys. J. **137**, 777 (1963).

[8] R. Hollerbach and R. R. Kerswell, J. Fluid Mech. **298**, 327 (1995).

[9] R. R. Kerswell, J. Fluid Mech. **298**, 311 (1995).

[10] K. D. Aldridge, Mathematika **19**, 163 (1972).

[11] D. H. Kelley, S. A. Triana, D. S. Zimmerman, A. Tilgner, and D. P. Lathrop, Geophys. Astrophys. Fluid Dyn. **101**, 469 (2007).

[12] E. Bullard and H. Gellman, Philos. Trans. R. Soc. London, Ser. A **247**, 213 (1954).

[13] R. T. Merrill, M. W. McElhinny, and P. L. McFadden, *The Magnetic Field of the Earth: Paleomagnetism, the Core, and the Deep Mantle*, International Geophysical Series, Vol. 63 (Academic Press, New York, 1996).

[14] A. M. Dziewonski and D. L. Anderson, Phys. Earth Planet. Inter. **25**, 297 (1981).

[15] H. S. Ribner, J. Acoust. Soc. Am. **29**, 435 (1957).

[16] M. Yamada and M. Okamura, J. Atmos. Sci. **41**, 2531 (1984).

[17] B. R. Sutherland, C. P. Caulfield, and W. R. Peltier, J. Atmos. Sci. **51**, 3261 (1994).

[18] K. Stewartson, J. Fluid Mech. **26**, 131 (1966).

[19] E. Dormy, P. Cardin, and D. Jault, Earth Planet. Sci. Lett. **160**, 15 (1998).

[20] K. D. Aldridge and A. Toomre, J. Fluid Mech. **37**, 307 (1969).

[21] S. Chandrasekhar, *Hydrodynamic and Hydromagnetic Stability* (Dover, New York, 1961).

[22] M. Rieutord and L. Valdettaro, J. Fluid Mech. **643**, 363 (2010.

[23] D. Schmitt, T. Alboussière, D. Brito, P. Cardin, N. Gagnière, D. Jault, and H. C. Nataf, J. Fluid Mech. **604**, 175 (2008).

[24] H.-C. Nataf and N. Gagniere, C. R. Phys. **9**, 702 (2008.

[25] J. Zhang, X. Song, Y. Li, P. G. Richards, X. Sun, and F. Waldhauser, Science **309**, 1357 (2005).

[26] X. Song and P. G. Richards, Nature (London) **382**, 221 (1996).

[27] W. L. Shew and D. P. Lathrop, Phys. Earth Planet. Inter. **153**, 136 (2005).

[28] S. Stergiopoulos and K. D. Aldridge, Phys. Earth Planet. Inter. **36**, 17 (1984).

[29] M. Rieutord, Phys. Earth Planet. Inter. **91**, 41 (1995).

[30] This case is similar to what is often called "geostrophic flow," in which Coriolis and pressure forces balance each other in a steady (time-independent) way.

[31] Though our device is a spherical shell, its modes are well approximated by the full-sphere modes, consistent with expectations from theoretical work [10,28]; in fact, some full-sphere modes persist unchanged in a spherical shell [6]. The change in geometry does have consequences, however, as will be discussed further below.

[32] Rotational forces in the calculations of [29] are weaker in the sense that the dimensionless Ekman number, $E = \nu \Omega^{-1} b^{-2}$, is larger. There $E = 10^{-5}$; in the experiments described here, $E \sim 10^{-7}$.